INT. J. NUM. METH. HEAT FLUID FLOW, VOL. 3, 245–256 (1993)

RECONSTRUCTION OF TEMPERATURE FIELDS FROM KNOWN BOUNDARY DATA USING COMPUTED TOMOGRAPHY

R. J. GU

Department of Mechanical Engineering, Oakland University, Rochester, Michigan 48309-4401, USA

AND

H. C. WANG

Department of Applied Mathematics, National Chung-Hsing University, Taiwan, Republic of China

ABSTRACT

A novel numerical technique is presented with which the temperature profile within a selected transverse plane of an object can be reconstructed provided the boundary data around the transverse plane are known. Numerical simulations of the proposed computed tomography technique are performed to verify its feasibility and accuracy using several heat conduction examples whose exact solutions can be found in literature. Restrictions of and mathematical difficulties encountered in the proposed technique are presented.

KEY WORDS Computed tomography Temperature fields Ill-posedness

INTRODUCTION

Majority of methods[1–6] developed to date to determine the internal temperature profile are valid when the objects of concern are transparent to light waves or exist in the form of either liquid or gas allowing the installation of mechanical probes within the objects. The need exists to develop a technique to detect internal temperature as the methods cited above fail. A novel technique using computed tomography (CT) is presented in this paper in which only the empirical thermal data are needed along the periphery of a selected cross-section of an object regardless of its form.

The CT technique in medical diagnosis is used to reconstruct the quantitative map of the X-ray attenuation coefficient in a transverse plane of a human body. Using an array of X-ray detectors the empirical data are collected from the X-ray transmitted through a human body at many different angles. Subsequently, the data are numerically processed to reconstruct the transversal image using the technique called filtered back-projection[7]. In this investigation, the proposed technique requires no X-ray or any other physical waves, the conventional means such as thermocouples may be employed to acquire the boundary data. Only fictitious rays are used in the mathematical formulation and numerical treatment.

Recently Wadley *et al.*[8] presented a tomographic technique using ultrasound to reconstruct the radially symmetric and rectangularly symmetric temperature fields within the stainless steel. Due to symmetry, only a few measurements of the ultrasonic time-of-flight are needed to

0961–5539/93/030245–12$2.00

Received April 1992
Revised January 1993

reconstruct the velocity profile. The data are then used to compute the temperature through a velocity–temperature relation.

Conventional numerical methods, such as finite difference, finite element, or boundary element, may be employed to determine the internal temperature of an object provided that the boundary conditions at *all* surface nodes *and* the material properties of the object under investigation are known. This is not so in the present CT technique in which only the boundary conditions along the periphery of a selected cross-sectional plane need to be prescribed. As a result, the CT technique only calculates the temperature at nodes in the selected plane. It needs to be pointed out that the current CT technique cannot be employed to solve the heat conduction problem. Rather, it is used to 'measure' the existing internal temperature distribution. Consequently, no material properties are required.

The formulation and numerical treatment of the CT technique using finite element method to approximate the tomographic integral equation are presented. Restrictions, undersampling and noise sensitivity of the CT technique are also discussed. Numerical simulation is demonstrated using several problems whose temperature solutions exist in closed form.

The present temperature reconstruction problem shares the mathematical analogy of ill-posedness with the other inverse problems[9]. In the latter problems, for instance, the surface temperature and heat flux are to be determined from the known temperature within the object. Ill-posedness of the CT technique is also discussed.

NUMERICAL TREATMENT OF THE CT TECHNIQUE

The problem of concern is depicted in *Figure 1* which represents a selected transverse plane of an object and an arbitrary fictitious X-ray intersecting the boundary at points 1 and 2 having known temperatures T_1 and T_2, respectively. The selected plane may be of a multiply-connected region as long as its boundary data are known. The jth fictitious X-ray in *Figure 1* may be expressed by the line equation:

$$y = m_j x + e_j \tag{1}$$

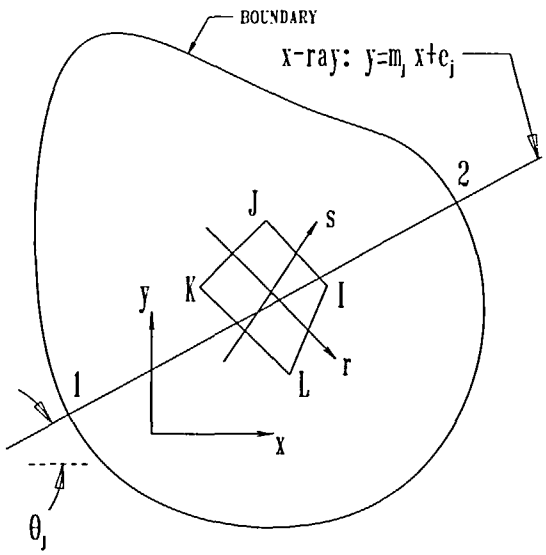

Figure 1 A selected transverse plane with a fictitious ray passing through a generic element

where m_j is the slope and e_j the y-intercept of the line. Since $dT = \partial T/\partial x\, dx + \partial T/\partial y\, dy + \partial T/\partial z\, dz$, integration of dT along the X-ray gives:

$$T_2 - T_1 = \int_{x_1}^{x_2} \left(\frac{\partial T}{\partial x} + m_j \frac{\partial T}{\partial y} \right) dx \tag{2}$$

where x_1 and x_2 are the x-coordinates of points 1 and 2, respectively. Note that the integration has to be carried out along the y-axis instead if the X-ray is parallel to the y-axis. It is readily seen that for (2) to remain valid the partial derivatives or the temperature gradients in (2) must be continuous throughout the region. This happens to be the major restriction of the present technique. Discontinuity of temperature gradients may stem from internal crack, material inhomogeneity, phase change, etc.

Our aim at this moment is to solve the integral equation (2) for the unknown temperature derivatives. In transmission CT used for medical diagnosis, the integrand in (2) appears to be the linear attenuation coefficient of the X-ray in human tissue. The integral equation represents the well-known Radon transform and the inverting technique widely used is called filtered back-projection[10]. Presently the integrand of (2) is, however, a function of the X-ray's incident angle. As a result, the method of filtered back-projection is unapplicable. Thus the following algebraic method is employed, which is in mathematical analogy with the simultaneous correction technique[11].

We first discretize the plane region into a number of four-noded elements. A generic element is shown in *Figure 1*. The temperature gradients in (2) may be approximated from element nodal values using the interpolation function H_i commonly found in finite element method[12]. Hence,

$$\frac{\partial T}{\partial x} = \sum_{i=1}^{4} H_i U_i \qquad \frac{\partial T}{\partial y} = \sum_{i=1}^{4} H_i V_i \tag{3}$$

where U_i and V_i are the nodal values of $\partial T/\partial x$ and $\partial T/\partial y$ at node i, respectively. Note that H_i is a linear interpolation function of the natural coordinates r and s. It thus entails a coordinate transformation from x–y to r–s in order to numerically evaluate the integral in (2). The coordinate transformation is fulfilled through the interpolation function as follows:

$$x = \sum_{i=1}^{4} H_i X_i \qquad y = \sum_{i=1}^{4} H_i Y_i \tag{4}$$

in which X_i and Y_i are the nodal coordinates. Substitution of (4) into (1) yields the X-ray equation in the transformed plane:

$$c_0 + c_1 r + c_2 s + c_3 rs = 0 \tag{5}$$

where $c_0, \ldots, c_3$ are constants. In general, c_3 does not vanish meaning that the fictitious X-ray in the transformed plane is not straight.

After discretization the integral equation (2) can be written as:

$$\sum_{n=1}^{K} \left[\int_{r_p^n}^{r_q^n} \sum_{i=1}^{4} (H_i U_i + m_j H_i V_i) J\, dr \right] = \Delta T_j \tag{6}$$

where:

$$J = \sum_{i=1}^{4} \left(\frac{\partial H_i}{\partial r} + \frac{\partial H_i}{\partial s} \frac{ds}{dr} \right) X_i$$

Here, $dx = J\, dr$. K is the total number of elements, r_p^n and r_q^n are, respectively, the r-coordinates of the two intersection points of the X-ray and the two edges of element n, and ΔT_j is the temperature differential, $T_2 - T_1$.

To numerically evaluate the integral by means of Gaussian quadrature, a linear transformation is needed to change the integration limits to $+1$ and -1. For a given value of r, the term ds/dr in J may be determined from (5). Since points 1 and 2 in *Figure 1* are not necessarily the element nodes, T_1 and T_2 need to be interpolated from the temperatures of their two neighbouring element nodes. It is found from our numerical experiments that satisfactory results can only be achieved provided the midside nodes on the boundary edges are inserted and the quadratic interpolation is adopted.

Each fictitious X-ray will produce one equation in the form of (6). One X-ray may result in two or more equations if a multiply-connected or convex region is involved. For an N-node model, there are $2N$ unknown nodal temperature gradients. It requires at least $2N$ rays at many different angles in order to find all the unknowns. Therefore (6) may be written in the following algebraic form:

$$\sum_{i=1}^{2N} A_{ji} Z_i = \Delta T_j \qquad j = 1, 2, \ldots, 2N \tag{7}$$

or in matrix form:

$$\mathbf{AZ} = \mathbf{D} \tag{8}$$

where $\mathbf{Z}^T = [U_1 \quad V_1 \ldots U_N \quad V_N]$, $D_j = \Delta T_j$, and A_{ji} are the coefficients of Z_i. Note that matrix **A** is non-symmetric and sparse, since there are only a few elements on the way of an incident X-ray.

If a total number of $2N$ rays are used in conjunction with some incident angles to produce a square matrix **A** in (8), the resulted solution is hardly acceptable. This phenomenon is commonly known as undersampling (too few data) in image processing. Ill-posedness also contributes to the failure of using a square matrix **A**, because two nearly parallel rays may produce two rows of practically identical components in **A** causing it to be nearly rank deficient. To overcome this mathematical hurdle, we consider the following procedure. As a matter of fact, inserting midside nodes on the boundary element edges is the first step taken to alleviate the ill-posedness. Then the total number of rays, M, is increased to twice as many, for instance, to tackle the problem of undersampling. As a consequence, we have a least-squares (LS) problem:

$$\min_{\mathbf{z}} \|\mathbf{AZ} - \mathbf{D}\| \tag{9}$$

where **A** is now an M-by-$2N$ rectangular matrix, **D** represents a vector of compatible size, and $\|\cdot\|$ indicates the vector norm. To solve this LS problem, there are a number of methods[13] at our disposal. First, in the method of normal equation, (8) is premultiplied by $\mathbf{A}^T$, the transpose of **A**. Then Gaussian elimination is utilized to find the unknown vector **Z**. As pointed out by Golub and Van Loan[13], Gaussian elimination in this numerical scheme may cause spurious errors. Thus the **QR** decomposition method using modified Gram–Schmidt algorithm is also considered. We have found in our numerical experiments that both methods give practically the same results.

Another measure to alleviate the ill-posedness of this LS problem is to specify the boundary temperature gradients, $\partial T/\partial z$ and $\partial T/\partial y$, in addition to the boundary temperature. As indicated by Tikhonov and Arsenin[14], non-uniqueness of an ill-posed problem may be eliminated provided further supplementary information pertaining to the problem is prescribed. On some heat conduction problems in which the boundary temperature is held constant and the transient-state solution is of interest, the boundary temperature gradients at an instance must be specified in order to uniquely determine the internal temperature corresponding to that specific instance. The temperature gradients or heat flux may be measured using the experimental techniques reported in the literature[15,16]. In axisymmetric cases, the boundary temperature around a selected plane normal to the axis of symmetry is uniform. Both nodal temperatures and temperature gradients must be specified to obtain a non-trivial solution. In addition, the following constraint

for each internal node with polar coordinates (ρ, θ) may be implemented to ensure axisymmetry:

$$\frac{\partial T}{\partial \theta} = 0$$

or,

$$\tan\theta \frac{\partial T}{\partial x} - \frac{\partial T}{\partial y} = 0 \tag{10}$$

Further constraints, such as the one that requires $\partial T/\partial \rho$ be equal at a constant ρ, may also be implemented. It is not considered, however, in this investigation. Consequently, matrix **A** of (8) must be modified to account for the known temperature gradients. This may be fulfilled by utilizing the so-called static condensation[12]. It modifies the RHS vector after eliminating the known temperature gradients. The method described in the previous paragraph is then used to solve for the remaining unknown temperature gradients at the internal nodes. The CT technique will produce erroneous trivial solutions in cases where the boundary temperature is uniform and the selected sectional boundary is insulated. Consider, for example, the axisymmetric problem of a solid cylinder with insulated cylindrical surface. This is because of the fact that the RHS vector **D** in (8) is unaffected after the static condensation implementing the insulation condition is performed. In this event, a different section should be selected, if possible.

We show in Appendix I that if a function can describe the temperature and temperature gradient on the boundary, this function must be the unique temperature field of the whole medium. This indicates that to obtain the valid solution both the temperature and temperature gradient on the boundary must be included in the current CT technique. As our experience shows, the CT technique performs rather well for problems having a monotonic temperature field and non-uniform boundary temperature, even though the boundary temperature gradient is not included. Care must be exercised in this regard, because whether the temperature field is monotonic is generally not known.

After the nodal temperature gradients have been found, the internal nodal temperatures may be calculated through the integration of dT over an element edge having a known nodal temperature at one end. For an element edge with slope m and end nodes i and j, we have

$$T_j = T_i + \int_{x_i}^{x_j} \left(\frac{\partial T}{\partial x} + m \frac{\partial T}{\partial y} \right) dx \tag{11}$$

where T_i is either given or found in the process, and x_i and x_j the x-coordinates of the end nodes. The derivatives in (11) need to be approximated using interpolation functions from the nodal temperature gradients found in the previous phase. Gaussian quadrature may then be used to evaluate the integral in (11). Note that an interior node is often the intersection of several element edges along which (11) is evaluated. The temperatures found for this intersection from different edges deviate slightly from each other, and their averaged value is used.

NUMERICAL EXPERIMENTS AND ERROR ANALYSIS

We now demonstrate three heat conduction examples whose exact temperature fields can be found in the text by Özişik[17]. In the first example, we are to reconstruct the steady-state temperature in a solid cylinder of length $L = 10$ m and radius $R = 4$ m, when its cylindrical surface dissipates heat by convection into a medium at zero temperature, the boundary at the upper end is kept at zero temperature, and the boundary at the lower end is kept at a radially symmetric temperature profile of $2(1 + \rho^2)$, where ρ is the radial coordinate. The profile at the lower end is chosen in such a way that a selected plane near the lower end will have a concave

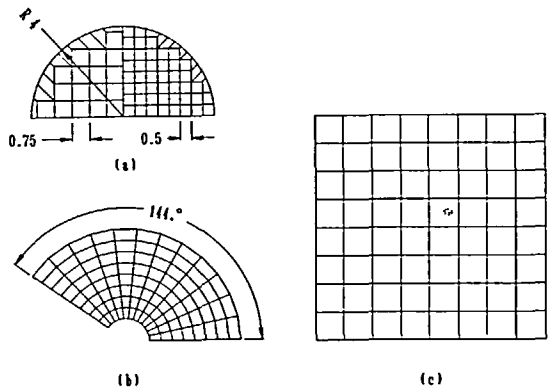

Figure 2 Meshes used for the three examples: (a) a solid cylinder, (b) portion of a hollow cylinder, (c) an orthotropic square region

internal temperature profile. Two meshes for the full circular region are used in reconstructing the temperature in a plane normal to the axial axis and 2 m from the lower end. A quarter of each mesh is shown in *Figure 2a*. The element size of the fine mesh with 250 nodes and 220 elements is about 44.4% of the coarse counterpart having 129 nodes and 108 elements. The exact solution is used to calculate the boundary temperature and temperature gradient to simulate the experimental measurements. The following data are arbitrarily chosen in the calculation: heat transfer coefficient = 1.0 W/m^2 C, and conductivity = 1.0 W/m C. The reconstructed temperature profile using the proposed technique is shown in *Figure 3* while *Table 1* contains the legend for the curves and the temperature at the centre of the cylinder for each numerical test. Note that the exact temperature at the centre is 6.941°C. The numerical tests are conducted using various combinations of d, the distance between two neighbouring parallel rays, and $\Delta\theta$, the incremental angular distance of the rays used. These curves represent the temperature profile along the diameter on the x-axis, except that curve 3b is for the diameter 45° from the x-axis. Note that curves 3a and 3b are the result of the numerical test 3 in *Table 1* which ignores (10). The predicted result using the coarse mesh, shown by curve 1 in *Figure 3*, does not reflect the concavity. By comparing curves 2, 3 and 7, it is seen that the predicted result is improved noticeably if (10) is implemented. Note that curve 2, produced using $d = 0.3$ and $\Delta\theta = 5°$, practically resembles the exact solution with a maximum error of less than 2%. Using the same combinations of d and $\Delta\theta$, some computer-generated random errors within a specified range, signified as A.E. (artificial error) in *Table 1*, are imposed on the boundary data to simulate the real situation. The contaminated boundary data do not represent the condition of axisymmetry, although (10) is enforced in the numerical tests 4, 5, 6, 8, 10, and 11 in *Table 1*. Note that tests 10 and 11 in *Table 1* are not plotted in *Figure 3*. Although these reconstructed temperature profiles from the contaminated data contain spurious errors of various degree, they display concavity. *Table 1* may be cross-referenced with the results reported later in *Table 2*.

More numerical tests are performed on this example to gain insight of the reconstruction technique. The results are displayed in *Table 2*. Here only the calculated temperature at the centre of the cylinder is included since it bears the degree of integrated error, and can be used as an accuracy indicator for the numerical tests. Note that the tests are run using (10) and the fine mesh in *Figure 2a* without any artificial errors. The tests are displayed in five groups by their values of $\Delta\theta$. Apparently, the group $\Delta\theta = 9°$ is not acceptable. This is known as θ-undersampling in the field of image reconstruction because too few angles are used. The reconstructed result deteriorates as the value of d increases in a group of tests. Generally the groups with $\Delta\theta = 5°$ and 7° predict better results. In the groups with $\Delta\theta = 1°$ and 3° the improvement stagnates as the value of d decreases.

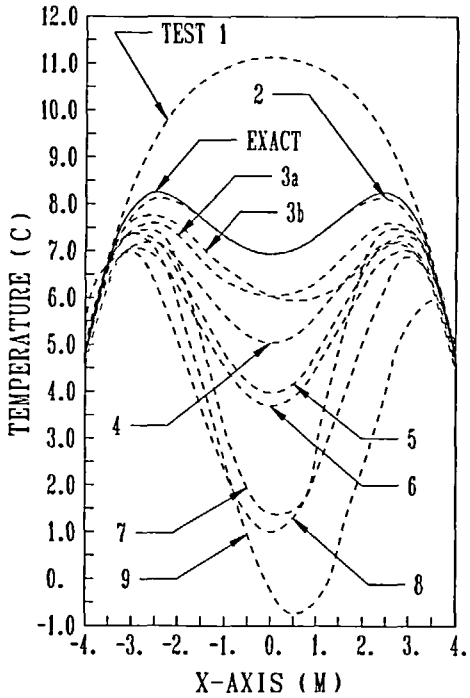

Figure 3 Reconstructed temperature profile for example 1, see *Table 1* for detailed legend

Table 1 Legend of curves in *Figure 3*

Test	$\Delta\theta$†	d	M	A.E. (%)	Eqn (10)	T_{centr}*	Mesh
1	3° (60)	0.3	1560		Yes	11.132	Coarse
2	5° (36)	0.3	936		Yes	6.944	Fine
3	3° (60)	0.15	3180		No	6.044	Fine
4	5° (36)	0.3	936	4–8	Yes	5.043	Fine
5	5° (36)	0.3	936	−4–4	Yes	3.975	Fine
6	5° (36)	0.3	936	0–8	Yes	3.697	Fine
7	5° (36)	0.3	936	—	No	1.401	Fine
8	5° (36)	0.3	936	−8–8	Yes	1.070	Fine
9	3° (60)	0.2	2340	−4–4	No	−0.210	Fine
10**	3° (60)	0.05	9540	−4–4	Yes	2.090	Fine
11**	1° (179)	0.1	13936	−4–4	Yes	2.033	Fine

†The resulted number of angles is given in parenthesis
*The exact temperature at the centre is 6.941°C
**Not plotted in *Figure 3*

The second example involves a hollow cylinder whose initial temperature is $T_0 > 0$, and the boundary surfaces at $R = R_i$ and $R = R_0$ are then held at zero temperature. We are to reconstruct the axisymmetric temperature field from the available boundary data at a specific instance. To demonstrate the capability of the CT technique in tackling irregular geometries, we choose an arbitrary portion of the cylinder, and simulate the boundary measurements using the exact solution. The following data are arbitrarily chosen: thermal diffusivity = 1.0×10^{-6} m^2/sec, $T_0 = 2$°C, $R_i = 1$ m and $R_0 = 5$ m. The only mesh used in the numerical tests is shown in *Figure*

Table 2 Undersampling analysis with different combinations of d and $\Delta\theta$ for example 1

Test	$\Delta\theta$	d	M	T_{centr}
1	1°	0.08	17456	6.177
2		0.1	13936	6.174
3		0.15	9360	6.064
4		0.2	6896	5.768
5		0.3	4608	5.932
6	3°	0.05	9540	6.020
7		0.1	4740	6.070
8		0.2	2340	5.709
9		0.3	1560	5.350
10		0.4	1140	2.626
11		0.5	900	0.372
12	5°	0.05	5724	6.161
13		0.1	2844	6.494
14		0.2	1404	6.324
15		0.3	936	6.944
16		0.4	684	7.438
17		0.5	540	−0.501
18	7°	0.05	4134	6.546
19		0.1	2054	6.604
20		0.2	1014	6.216
21		0.3	676	6.683
22		0.4	494	−1.269
23	9°	0.05	3180	2.998
24		0.1	1580	3.440
25		0.2	780	1.689
26		0.3	520	4.834
27		0.4	380	8.516

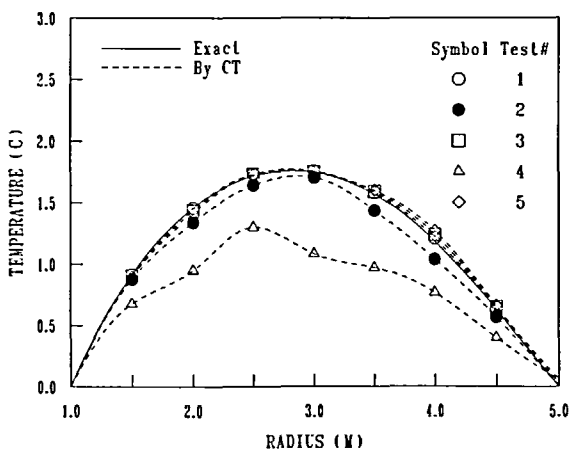

Figure 4 Reconstructed temperature profile for example 2, see *Table 3* for detailed legend

2b which has 117 nodes and 96 elements. The reconstructed temperature profile at an arbitrary instance along the radial line at $\theta = 72°$ is shown in *Figure 4*. In the calculation $\Delta\theta = 4°$ and $d = 0.4$ m are used. The legend for the curves is given in *Table 3* together with the maximum percentage error at a node (not necessarily of the same location). The last four tests in *Table 3* are not plotted in *Figure 4*. Although many more rays are used in the last four tests, they do

Table 3 Legend of curves in *Figure 4*

Test	$\Delta\theta$	d	M	A.E. (%)	Eqn (10)	Max. error (%)
1	4°	0.4	780	—	Yes	2.25
2	4°	0.4	780	—	No	12.26
3	4°	0.4	780	−4–4	Yes	4.97
4	4°	0.4	780	−8–8	No	48.64
5	4°	0.4	780	−8–8	Yes	7.92
6*	3°	0.2	2113	—	Yes	1.94
7*	3°	0.2	2113	−4–4	Yes	4.82
8*	3°	0.2	2113	−8–8	Yes	7.78
9*	3°	0.2	2113	−8–8	No	66.19

*Not plotted in *Figure 4*

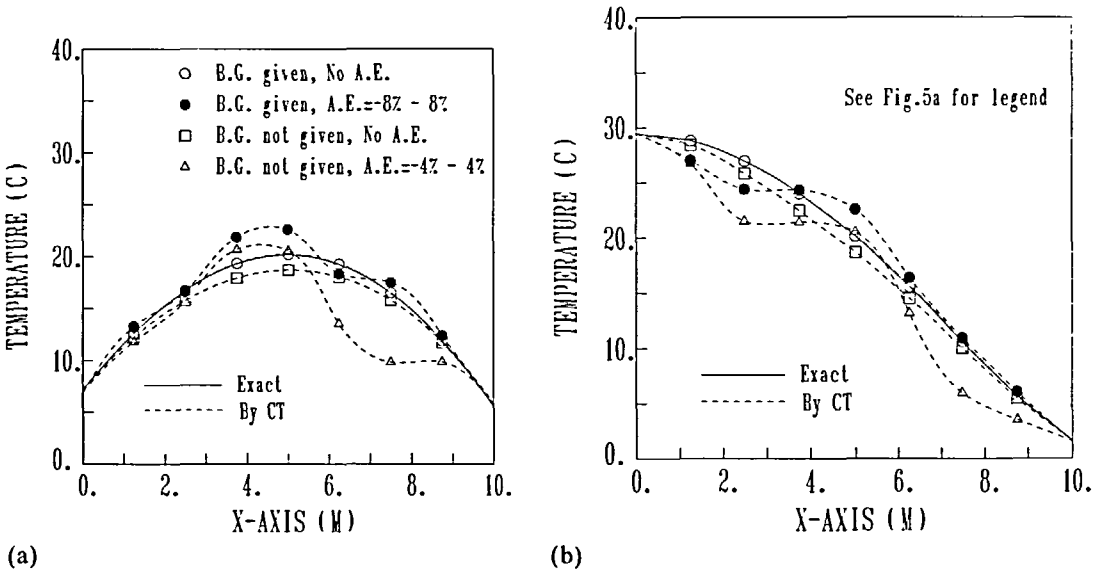

Figure 5 Reconstructed temperature profile for example 3: (a) temperature along the −45° diagonal, (b) temperature along the 45° diagonal. Note: A.E. = artificial error; B.G. = boundary gradient

not show any significant discrepancy from the first five. Since the cylindrical surface has zero temperature, the computer-generated random error as a percentage is imposed only on the boundary temperature gradient.

In the third example the steady-state heat conduction for an orthotropic rectangular region, $0 \leqslant x \leqslant a$, $0 \leqslant y \leqslant b$, is considered. The region is heated by a constant heat source g_0 (W/m^3), while the boundaries at $x = 0$ and $y = 0$ are kept insulated and those at $x = a$ and $y = b$ are dissipating heat by convection into an environment at zero temperature. The following data are chosen to calculate the exact boundary temperature and temperature gradient: $g_0 = 1.0$ W/m^3, heat transfer coefficient in both directions = 1.0 W/m^2 C, conductivity in (x, y) directions = (1.0, 1.5) W/m C, and $a = b = 10$ m. Although the material of concern is orthotropic, it is homogeneous. Thus the continuity of the temperature derivatives is ensured. The mesh having 64 elements and 81 nodes is shown in *Figure 2c*. The reconstructed temperature profiles along the −45° and 45° diagonals are depicted in *Figures 5a* and *5b*, respectively. The legend given in *Figure 5a* is also applicable for *Figure 5b*. All tests are run using the combination of $d = 0.8$ m

and $\Delta\theta = 6°$ which results in 458 rays. Curve 1 of both *Figures 5a* and *5b* agrees rather well with the exact solution. Since this problem has a monotonic temperature field and non-uniform boundary temperature, tests are also run without specifying the nodal boundary gradients (indicated as B.G. in *Figure 5a*). Curve 3 contains the maximum percentage error of 7.3% at the geometric centre. It is seen from curve 4 that the CT scheme is more sensitive to errors if no boundary gradient is specified.

CONCLUSION

A computerized tomographic technique is developed to reconstruct the temperature field within a selected transverse plane of an object if the temperature and temperature gradient around the periphery of the selected plane are provided. The technique requires that the temperature derivatives, $\partial T/\partial x$ and $\partial T/\partial y$, be continuous within the selected cross-section. Numerical treatment of the formulated integral equation and the procedures taken to circumvent the mathematical difficulties regarding ill-posedness are presented. We show that to obtain a unique solution, both the temperature and temperature gradient must be specified on the periphery of the selected cross-sectional plane. At this stage of research, only numerical simulations are performed. The exact solutions of three heat conduction problems are used to simulate the empirical measurements at the boundary. The numerical results using the CT technique are in good agreement with the exact solutions. We have also tested some other examples of Özişik[17], all result in a similar degree of success. Our future study may include exploring methods to improve the CT technique, statistical methods to smooth data noise, and investigating factors affecting the accuracy of the CT technique. It is well understood from the analysis that the proposed technique may fail if the difficulty in attaining accurate data, both boundary temperature and temperature gradient, in the laboratory cannot be overcome. Therefore what lies ahead is a great challenge for us to verify the technique in the laboratory.

ACKNOWLEDGEMENT

The study is supported by the National Science Council, Taiwan, ROC, through grant NSC 80-0401-E-005-11.

REFERENCES

1 Blinkov, G. N., Fomin, N. A., Rolin, M. N., Soloukhin, R. I., Vitkin, D. E. and Yadrevskaya, N. L. Speckle tomography of a gas flame, *Exp. Fluids* **8**, 72–76 (1989)
2 Kajanto, I. and Friberg, A. T. A silicon-based fiber-optic temperature sensor, *J. Phys. (E)* **21**, 652–656 (1988)
3 Liu, T. C., Merzkirch, W. and Obserste-Lehn, K. Optical tomography applied to speckle photographic measurement of asymmetric flows with variable density, *Exp. Fluids*, **7**, 157–163 (1989)
4 Sweeny, D. W. and Vest, C. M. Reconstruction of three-dimensional refractive index fields from multidirectional interferometric data, *Appl. Opt.* **12**, 2649–2664 (1973)
5 Takahashi, T., Katsuki, M. and Mizutani, Y. Measurement of flame temperature by optical fiber thermometer, *Exp Fluids* **5**, 514–520 (1988)
6 Venkateshan, S. P., Shakkottai, P., Kwack, E. Y. and Back, L. H. Acoustic temperature profile measurement technique for large combustion chambers, *J. Heat Transfer* **111**, 461–466 (1989)
7 Morgan, C. L. *Basic Principles of Computed Tomography*, University Park Press, Baltimore (1983)
8 Wadley, H. N. G., Norton, S. J., Mauer, F. and Droney, B. Ultrasonic measurements of internal temperature distribution, *Phil. Trans. R. Soc. Lond.* **A320**, 341–361 (1986)
9 Beck, J. V., Blackwell, B. and St. Clair, C. R. *Inverse Heat Conduction. Ill-posed Problems*, Wiley, New York (1985)
10 Brooks, R. A. Computational principles of transmission CT, in *Medical Physics of CT and Ultrasound: Tissue Imaging and Characterization* (Eds. G. D. Fullerton and J. A. Zagzebski), pp. 37–52 (1980)
11 Brooks, R. A. and Di Chiro, G. Principles of computer assisted tomography (CAT) in radiographic and radioisotopic imaging, *Phys. Med. Biol.* **21**, 689–732 (1976)
12 Cook, R. D., Malkus, D. S. and Plesha, M. E. *Concepts and Applications of Finite Element Analysis*, 3rd Edn, Wiley, New York (1989)

13 Golub, G. H. and Van Loan, C. F. *Matrix Computations*, 2nd Edn, Johns Hopkins University Press, Baltimore (1989)
14 Tikhonov, A. N. and Arsenin, V. Y. *Solution of Ill-Posed Problems*, Wiley, New York (1977)
15 Beasley, D. E. and Figliola, R. S. A generalized analysis of a local heat flux probe, *J. Phys. (E)* **21**, 316–322 (1988)
16 Shewen, E. C., Hollands, K. G. T. and Raithby, G. D. The measurement of surface heat flux using the Peltier effect, *J. Heat Transfer* **111**, 798–803 (1989)
17 Özişik, M. N. *Heat Conduction*, Wiley, New York (1980)
18 Brebbia, C. A., Telles, J. C. F. and Wrobel, L. C. *Boundary Element Techniques: Theory and Applications in Engineering*, Springer-Verlag, Berlin, Heidelberg (1984)
19 Banerjee, P. K. and Butterfield, R. *Boundary Element Methods in Engineering Science*, McGraw-Hill, London (1981)

APPENDIX I

Proof of uniqueness

Consider the following well-posed boundary value problem:

$$\begin{aligned} A(\theta) &= p(x) \qquad x \in \Omega \\ \theta &= r(x) \qquad x \in \Gamma_1 \\ B(\theta) &= s(x) \qquad x \in \Gamma_2 \end{aligned} \tag{A1}$$

where $A(\ )$ is the differential operator for the heat equation, $\theta(x)$ the unknown function, $B(\ )$ the differential operator defining the Neumann or mixed type boundary condition, and $p(x)$, $r(x)$, and $s(x)$ the prescribed functions within domain Ω and on the boundaries Γ_1 and Γ_2. Although the boundary conditions may appear in different forms, it should not affect the consequences of this development.

Provided that the function $\theta(x)$ has been determined from the above boundary value problem, the following relations may be established:

$$\theta = f(x) \qquad x \in \Gamma \tag{A2}$$

$$\frac{\partial \theta}{\partial n} = g(x) \qquad x \in \Gamma \tag{A3}$$

where $\Gamma = \Gamma_1 \cup \Gamma_2$, and n is the unit outward normal to Γ. We will show in this Appendix that, if there exists a function ϕ such that:

$$\phi = \theta = f(x) \qquad x \in \Gamma \tag{A4}$$

$$\frac{\partial \phi}{\partial n} = \frac{\partial \theta}{\partial n} = g(x) \qquad x \in \Gamma \tag{A5}$$

then ϕ must be the solution to the above boundary value problem (A1). To achieve this we begin with the following theorem.

Theorem: Let function $\alpha(x)$ be the solution to the following boundary value problem:

$$\begin{aligned} A(\alpha) &= q(x) \qquad x \in \Omega \\ \alpha(x) &= 0 \qquad x \in \Gamma \end{aligned}$$

If $\partial\alpha/\partial n = 0$ on Γ, then $q(x) = 0$ and $\alpha(x) = 0$ within Ω.

Proof: It is known from the boundary integral equation approach[18,19] that the function α can be written as:

$$\alpha(\xi) = \int_\Gamma [\alpha(x)F(x, \xi) - \beta(x)G(x, \xi)]\, d\Gamma(x) + \int_\Omega q(x)G(x, \xi)\, d\Omega(x) \qquad \xi \in \Omega \tag{A6}$$

and

$$c\alpha(\xi_0) = \int_\Gamma [\alpha(x)F(x, \xi_0) - \beta(x)G(x, \xi_0)]\, d\Gamma(x) + \int_\Omega q(x)G(x, \xi_0)\, d\Omega(x) \qquad \xi_0 \in \Gamma \tag{A7}$$

where

$$\beta(x) = -k\frac{\partial \alpha(x)}{\partial n}$$

Here, $G(x, \xi)$ is the singular solution for the temperature at x generated by a unit point source applied at ξ in an infinite space, and $F(x, \xi)$ the corresponding heat flux due to $G(x, \xi)$*, c a geometry parameter depending on the surface smoothness at ξ_0, and k the conductivity. Since we have $\alpha = \partial\alpha/\partial n = 0$ on boundary Γ, (A7) becomes:

$$\int_\Omega q(x)G(x, \xi_0)\mathrm{d}\Omega(x) = 0 \qquad \xi_0 \in \Gamma$$

For this to be true, we must have $q(x) = 0$. As a result, it is readily seen from (A6) that $\alpha(\xi) = 0$ for all the points ξ within domain Ω. This completes the proof of the theorem.

Now let

$$\gamma(x) = \theta(x) - \phi(x)$$

where function $\theta(x)$ is the solution to the boundary value problem (A1) and satisfies the conditions (A2) and (A3), and function $\phi(x)$ is chosen to satisfy the conditions (A4) and (A5). After applying the differential operator $A(\ )$ on $\gamma(x)$, we have the following:

$$A(\gamma) = Q(x) \qquad x \in \Omega$$

and

$$\gamma = \frac{\partial\gamma}{\partial n} = 0 \qquad x \in \Gamma$$

According to the above theorem we have then $Q(x) = 0$ and $\gamma(x) = 0$ for $x \in \Omega$. Hence we conclude that the function $\phi(x)$ chosen to satisfy the conditions (A4) and (A5) must be identical to the solution $\theta(x)$ of the boundary value problem (A1).

In this Appendix we have assumed isotropy for the medium and considered only the steady-state solution. Following the technique outlined here, we may achieve similar results for problems involving anisotropic and transient state using the treatments as depicted in References 18 and 19.

*For brevity, the complete forms of $G(x, \xi)$ and $F(x, \xi)$ are not included here, although they may be found in References 18 and 19.